



SEMESTER PROJECT

LAI LABORATORY

Simulation and implementation of a Wireless Power Module for dielectric elastomer actuator

Tomas Garate Anderegg

Supervised by Maribel Caceres Rivera

Prof. Yves Perriard and Paolo Germano

June 6, 2025

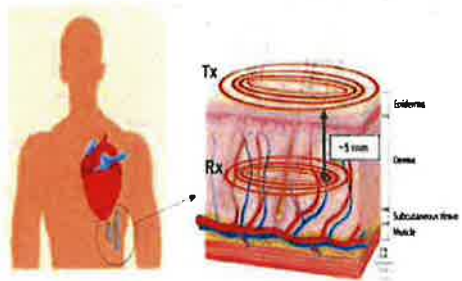
Neuchâtel, Microcity EPFL

SEMESTER PROJECT, SECTION DE MICROMECHANIQUE – SMT, SPRING 2024-2025

Tomas Joaquin GARATE ANDEREgg

Simulation and implementation of a wireless power module for dielectric elastomer actuator

Many applications for implantable devices requires a battery to operate. Such batteries present various limitation for long term transcutaneous devices. More and more application for implantable devices uses wireless power technologies, what present a reliable solution in health application as ventricular assistance devices, neuroimplants, eye power lens, and etc. In this project the goal is to develop a wireless implantable module that allows to transfer energy from a transmitter on the outside to the receiver inside the skin; to provide energy to a Dielectric Elastomer actuator.

**Objectives of the work**

The objectives of the project are to:

- Model and design a wireless power transmitter and receiver coil.
- Consider dimensions, tuning of parameters, and low power consumption (maximum of 600mW).
- Model the behavior of the transmission considering the tissue as a medium 5-10 [mm].
- Estimate and measure losses, and the efficiency of the wireless power system.

Report

The final report will contain the following points:

- Justification of the chosen topology for wireless power based on the requirements and state of the art.
- Simulation of the selected topology and reasoning of parameters (inductance, capacitance, and parasitics).
- Measurements comparing the simulations and experimental results of wireless power system.
- Limitation of the Implementation.
- Conclusion and Future work.

References

- [1] K. N. Bocan, M. H. Mickle and E. Sejdic, "Multi-Disciplinary Challenges in Tissue Modeling for Wireless Electromagnetic Powering: A Review,"
- [2] Khan, S.R.; Pavuluri, S.K.; Cummins, G.; Desmulliez, M.P.Y. Wireless Power Transfer Techniques for Implantable Medical Devices: A Review
- [3] Zhang, J., Das, R., Zhao, J., Mirzai, N., Mercer, J., & Heidari, H. (2022). Battery-free and wireless technologies for cardiovascular implantable medical devices. *Advanced Materials Technologies*, 7(6), 2101086.

Supervisor: Maribel Caceres Rivera

Maribel Caceres Rivera

Professor: Yves Perriard

Yves Perriard

During the first week, a weekly meeting will be set with the supervisor(s) and the Professor. Furthermore, an intermediate assessment meeting will be set at the mid-semester.

Contents

1	Introduction	4
1.1	Problem Context	4
1.2	Objectives	4
1.3	State of the Art	4
2	Assumptions	6
3	Approach Used	7
3.1	Determination of Resonant Circuit Parameters	7
3.2	Coil Design Based on Target Inductance	9
3.3	PCB Layout and Design	10
3.4	Fabrication and Validation of Inductance	10
3.5	Circuit Assembly and Resonance Verification	12
3.6	Power Transfer Characterization	14
3.7	Efficiency Analysis	14
4	Description of Solutions	17
5	Comparative Results	22
6	Critique of Solutions	23
7	Conclusion	24

1 Introduction

1.1 Problem Context

Many applications for implantable devices rely on batteries for operation. However, these batteries present various limitations for long term transcutaneous devices, particularly for individuals who require surgery to replace them, which poses a high risk. Increasingly, applications for implantable devices are turning to Wireless Power Technologies (WPT), offering a reliable solution for health applications such as ventricular assist devices, neuro implants, and intraocular lenses, among others [1, 4].

1.2 Objectives

The goal of this semester project is to develop a wireless implantable module that enables energy transfer from an external transmitter to a receiver inside the skin, thereby providing power to a Dielectric Elastomer Actuator (DEA).

1.3 State of the Art

Nowadays, various Wireless Power Transfer (WPT) techniques exist working with different physical phenomena. As shown in Figure 1, several approaches can be used to transfer energy. WPT techniques generally divided into two main categories: Electromagnetic (EM) and Non-Electromagnetic (Non-EM). Each category include different methods such as optical and acoustic for Non-EM, and capacitance or inductive coupling for EM.

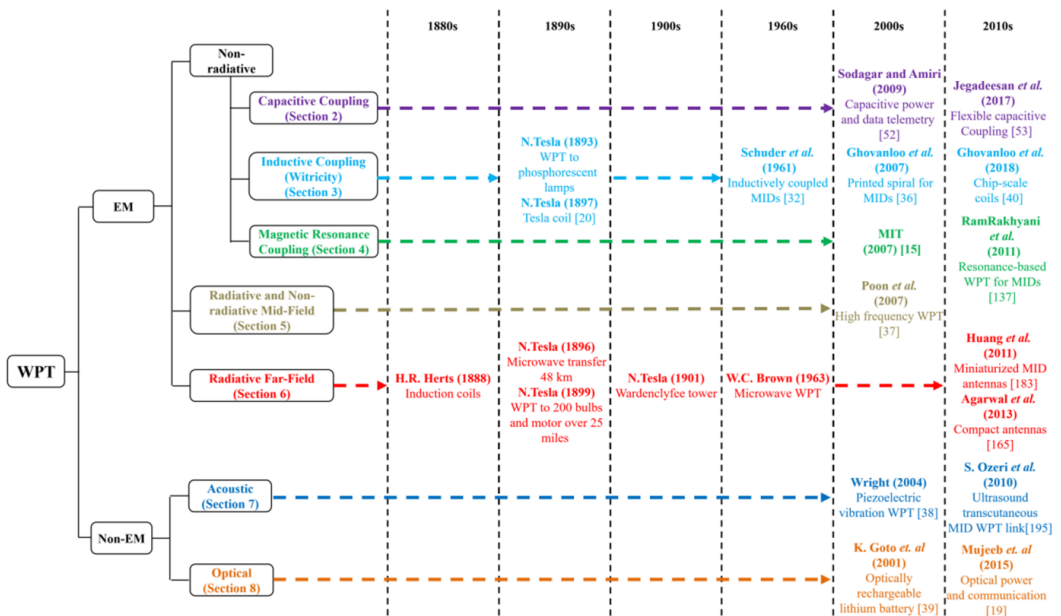


Figure 1: Classification and research overview of Wireless Power Transfer techniques indicating the key milestones relevant to implantable medical devices [8].

Each technique presents specific advantages and disadvantages. Considering my preferences,

I selected three techniques and outlined their respective pros and cons.

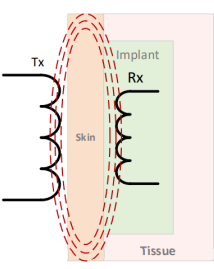
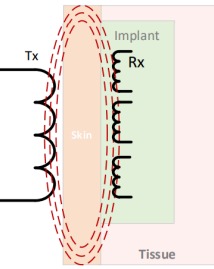
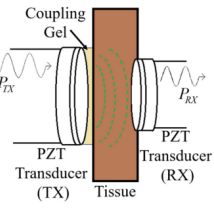
Technique	Advantages	Disadvantages
NRIC 	<ul style="list-style-type: none"> Well studied technique. Simple coil architecture makes it easy to manufacture. Provide a good Power Transfer Energy (PTE). Efficient technique for small distances. 	<ul style="list-style-type: none"> Not robust to misalignments. More complexe coil geometry can improve PTE. Frequency splitting phenomenon.
NRMRC 	<ul style="list-style-type: none"> Better performance characteristics in term of quality factor(Q) and higher bandwidth of operation. Improvement of the misalignment depending on the topology. 	<ul style="list-style-type: none"> More complexe architecture and manufacture. Requires more space. Frequency splitting phenomenon.
APT 	<ul style="list-style-type: none"> Better performance in terms of PTE than NRIC and NRMRC. For highly directional transmission, APT enables more compact design. 	<ul style="list-style-type: none"> Under-studied effect on the body. Complexity in manufacturing. Misalignment problems.

Table 1: Comparison of selected techniques: NRIC [2, 8, 12], NRMRC [2, 8, 14], APT [8, 16]

To choose the most suitable WPT method among Non-Radiative Inductive Coupling (NRIC), Non-Radiative Magnetic Resonance Coupling (NRMRC) and finally Acoustic Power Transfer (APT), Table 1 summarizes the respective advantages and disadvantages of each technique. Based on this comparison and the time constraints of the project, NRIC was selected as the most appropriate approach. In particular, the Serial-Serial (SS) compensation topology demonstrates good results in power transfer energy (PTE) when the receiver (Rx) and transmitter (Tx) are similar [15].

2 Assumptions

Before initiating the coil design process, several key constraints and assumptions must be defined to ensure an effective design. Two critical factors to address early are the physical size of the system and the power requirements.

In biomedical applications, wireless power transfer (WPT) devices vary in size depending on their target. For instance, inductive systems for brain applications typically range from 1.2 mm to 4 mm in diameter [8], while ocular systems fall between 9 mm to 20 mm [8]. In this project, the expected receiver (Rx) coil diameter is between 3 cm and 10 cm [5], based on similar literature. Since the Rx coil is implanted, minimizing its size is crucial to reduce patient invasiveness.

To support biomedical integration and limit the device profile, a planar circular coil was selected. Compared to solenoidal designs, planar coils offer a compact, low profile geometry suitable for subcutaneous placement. Only circular planar geometries are considered in this work.

Aside from size, power transfer is another key parameter. The system is expected to deliver between 300 mW and 500 mW to the load, ensuring proper operation of the implanted device.

Another major design choice is the operating frequency. A frequency of 13.56 MHz was selected, a common choice in biomedical WPT due to its balance between safety, efficiency and regulatory compliance [2, 4, 8]. Frequencies below 20 MHz are generally preferred to minimize tissue heating and improve penetration depth [6, 11, 20]. Although higher frequencies can improve efficiency, they pose safety risks due to increased tissue heating. Thus, 13.56 MHz offers a good trade-off.

However, operating at high frequency also introduces specific design challenges, particularly related to parasitic effects. In high frequency WPT systems, parasitic effects, series resistance and capacitance, must not be ignored. These parasitic directly influence the system's resonance behavior and efficiency. If ignored, parasitic capacitance can shift the resonant frequency away from the target 13.56 MHz, while parasitic resistance contributes to power losses, degrading the efficiency. During the coil design phase, it is essential to account for these effects to ensure optimal performance. To reduce the impact of the parasitic capacitance, we make sure that the total capacitance in the circuit is much larger than the estimated parasitic capacitance. Based on the literature, we estimate the parasitic capacitance to lie within the range of 2 to 5 pF [9, 13]. The parasitic resistance is calculated during the simulation based on the coil's geometry. Parasitic resistance is also influenced by skin depth and proximity effects at high frequencies, as shown in Eq. 3.3 in [19]. However, in this project, we only consider the DC resistance based on the coil's geometry, as the contributions from these high frequencies effects are minimal at our target frequency and can be neglected.

3 Approach Used

The design and testing process for the wireless power transfer (WPT) system followed a structured and iterative methodology, comprising several key stages:

3.1 Determination of Resonant Circuit Parameters

The first step involved determining the component values required to achieve resonance at the target frequency, ensuring proper circuit behavior and functionality. The system of Eq. 1, which includes the expression for the resonant frequency, quality factor and a fixed parasitic resistance R_p of 1Ω , was used to generate Figure 2 at $f_0 = 13.56$ MHz. In this analysis, a sweep of capacitance values was performed to identify an optimal range using an elbow method. This initial estimate provided a practical starting point for capacitor selection and its corresponding quality factor value. The chosen value was then slightly increased to ensure that it would remain significantly greater than the estimated parasitic capacitance, $C_{p,min} = 20$ pF, preventing parasitic effects from dominating the circuit's behavior. However, increasing the capacitance to avoid parasitic effects comes at the cost of a reduced quality factor. This trade-off is acceptable at this stage, as ensuring circuit stability and minimizing parasitic influence are prioritized over achieving the highest possible Q .

$$\begin{cases} f_0 = \frac{1}{2\pi\sqrt{LC}} \\ Q = \frac{\omega_0 L}{R} \\ R_p = 1 \Omega \end{cases} \quad (1)$$

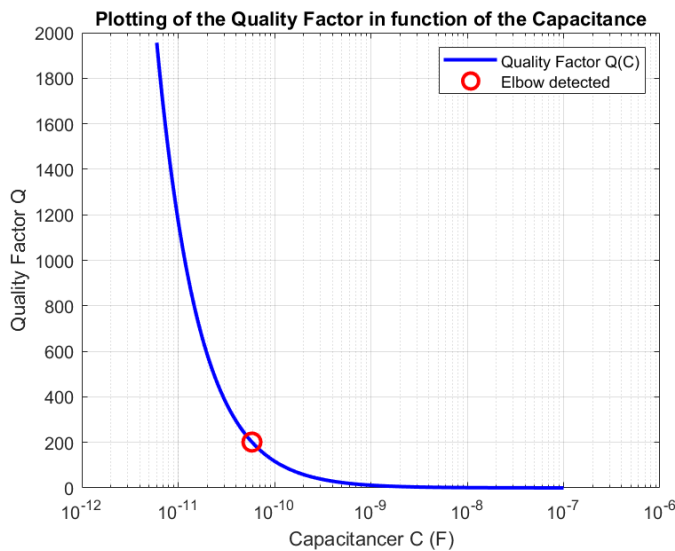


Figure 2: Plot of different values of the capacitance C over the quality factor Q in order to find the best trade-off.

Parameter	Not adjusted values	Adjusted values
Inductance (μH)	2.36	1.75
Capacitance (pF)	53.3	73.3
Quality Factor: Q	201.32	149.9

Table 2: First estimation of the values and adjusted values of inductance, capacitance and quality factor.

Once the capacitance value was selected, the corresponding inductance was calculated using the resonant frequency formula from system 1. Table 2 shows the values of capacitance, inductance and quality factor before and after adjusting the capacitance. These values defined the inductance and capacitance for both the transmitter and receiver circuits, as a symmetrical design, i.e. Rx and Tx have the same coil geometry, was implemented in this project. An initial schematic of the resonant circuit was built and simulated using LTSpice to validate the expected resonance behavior.

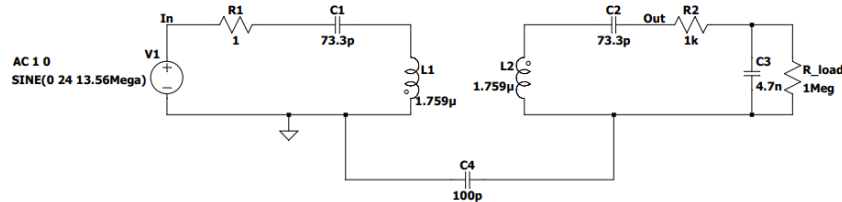


Figure 3: Circuit implementation with values on LTSpice.

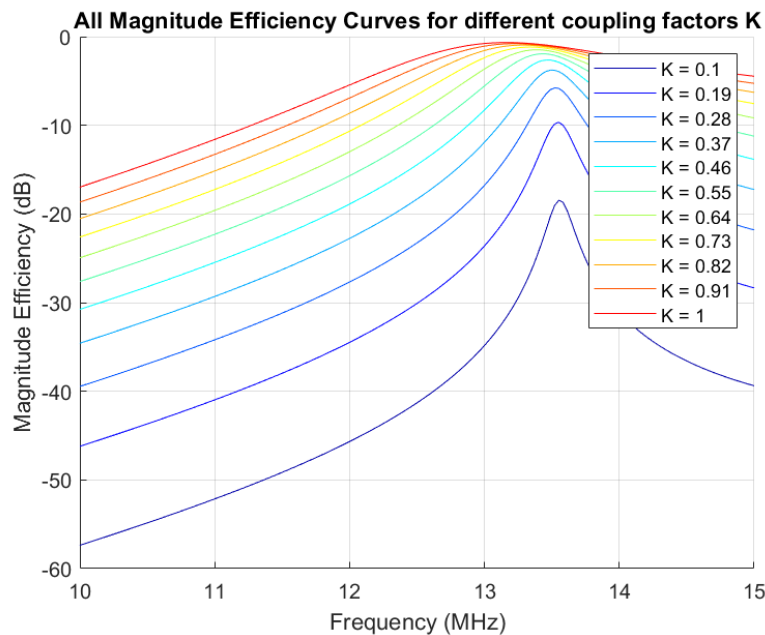


Figure 4: Results of the same circuit for different coupling factors (K) on LTSpice.

3.2 Coil Design Based on Target Inductance

Once the required inductance values were confirmed through simulation, the next stage focused on defining the coil geometry to physically realize those values. A MATLAB script was developed to generate multiple combinations of geometric parameters, such as the number of turns (N), track width (w) and diameters, that would result in the desired inductance based on the following expression:

$$L = \frac{\mu n^2 d_{avg} c_1}{2} \left(\ln \left(\frac{c_2}{\rho} \right) + c_3 \rho + c_4 \rho^4 \right) \quad (2)$$

This formula is based on the Current Sheet Approximation method described in [10] and provides a simple and accurate estimation of the inductance of circular spiral coils. The parameters are defined as follows:

- μ : permeability constant,
- n : number of turns in the spiral,
- $d_{avg} = \frac{d_{out}+d_{in}}{2}$: average diameter of the coil,
- $\rho = \frac{d_{out}-d_{in}}{d_{out}+d_{in}}$: fill ratio,
- C_1, C_2, C_3 and C_4 : empirical constants specific to the geometry of the spiral (for a circular layout: $C_1 = 1.0, C_2 = 2.46, C_3 = 0.0, C_4 = 0.2$).

This expression was used to systematically evaluate candidate coil geometries and select a configuration that satisfies the inductance value but also optimizes the coil parameters to maximize the electromagnetic field. An estimate of the parasitic resistance is also provided.

Table of the different geometrical parameters of the 'inductor' :

L (μH)	w (μm)	d_out (cm)	d_in (cm)	N	s (μm)	R (Ω)
1.76	526.32	4.83	4.33	4	121.05	0.525057
1.76	552.63	4.88	4.36	4	121.05	0.504418
1.76	605.26	4.21	3.28	5	405.26	0.466815
1.76	684.21	4.10	3.24	5	215.79	0.404710
1.76	684.21	4.38	3.34	5	452.63	0.425437
1.76	710.53	4.14	3.26	5	215.79	0.392612
1.76	736.84	4.18	3.27	5	215.79	0.381378
1.76	894.74	4.41	3.35	5	215.79	0.327001
1.76	921.05	4.51	3.37	5	263.16	0.322472
1.76	921.05	4.69	3.42	5	428.95	0.331927
1.76	947.37	4.09	2.53	6	428.95	0.315930
1.76	947.37	4.35	3.33	5	97.37	0.305686
1.76	947.37	4.52	3.38	5	239.47	0.314025
1.76	947.37	4.70	3.43	5	405.26	0.323217
1.76	947.37	4.75	3.44	5	452.63	0.325729

Figure 5: Circuit implementation with values found on LTSpice.

Table 5 provides a representative output of the MATLAB script, displaying different combinations of geometric parameters that satisfy the target inductance value. To guide the selection process, particular attention is given to the number of turns N and the track width

w . A higher number of turns generally allows more magnetic energy to be stored in the coil. Meanwhile, a large track width reduces the electrical resistance, which helps minimize Joule losses and allows higher current to flow more efficiently.

Finally, it is important to check the availability of the selected capacitance value, as exact values may not always be commercially available. Once a capacitance value close to the calculated one is identified and confirmed to be practically available, the other circuit components should be fine-tuned accordingly to maintain resonance at the target frequency. Table 3 shows the selected values used for the coil design based on a commercially available capacitance value.

Inductance (μH)	w (mm)	d_{out} (mm)	d_{in} (mm)	N	s (mm)
1.84	0.97	40.4	1.6	11.0	0.87

Table 3: Final values for the coil design with w : width, d_{out} : outer diameter, d_{in} : inner diameter, N : number of turns and s : spacing.

3.3 PCB Layout and Design

After validating the coil geometry, the layout was designed using KiCAD. The PCB design included additional pads and testing points to allow for future adjustments, such as adding external capacitors or testing alternative matching topologies. Provisions were also made for connector outputs and measurement access points for use with a network analyzer.

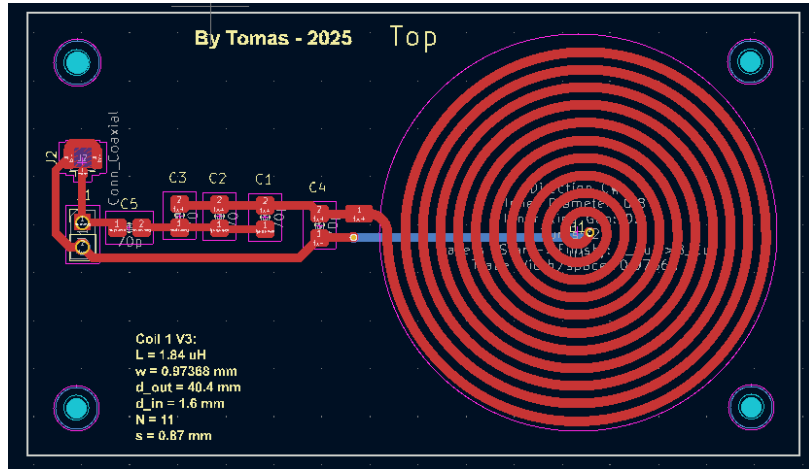


Figure 6: PCB layout designed using KiCAD.

3.4 Fabrication and Validation of Inductance

Upon receiving the fabricated PCB, the actual inductance of the coil was measured using an impedance meter as shown in Figure 7.

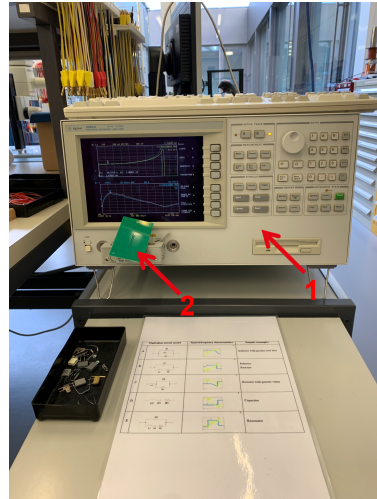


Figure 7: Impedance meter: Agilent 4294A Precision Impedance Analyzer, 40 Hz - 110 MHz (1) with PCB (2).

The impedance analyzer was configured to match the coil's characteristics as shown in Figure 8, allowing it to compute the equivalent inductance L_1 , capacitance C_1 and resistance R_1 .

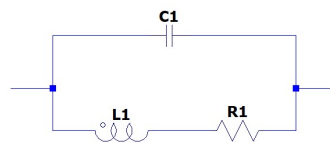


Figure 8: Model used in the impedance meter.

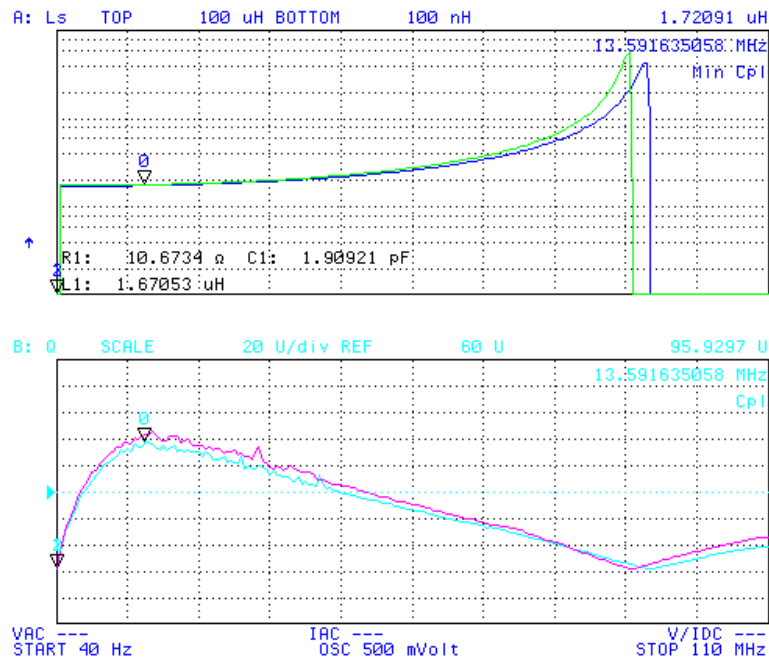


Figure 9: The top graph shows the variation of inductance across frequencies, while the bottom graph illustrates the corresponding evolution of the quality factor (Q) across frequencies.

Figure 9 illustrates the measured inductance of the coil across a range of frequencies. At the target operating frequency of 13.56 MHz, the inductance is approximately $1.72 \mu\text{H}$, which corresponds to a relative error of about 6.52 % compared to the theoretical value.

Additionally, the coil resistance is observed to be close to 1Ω at 13.56 MHz, validating the assumption made earlier in the design process about the parasitic resistance.

Once the actual inductance was confirmed, the required capacitance values were recalculated to ensure the circuit resonates precisely at the target frequency as suggested by the Figure 10 and 11.

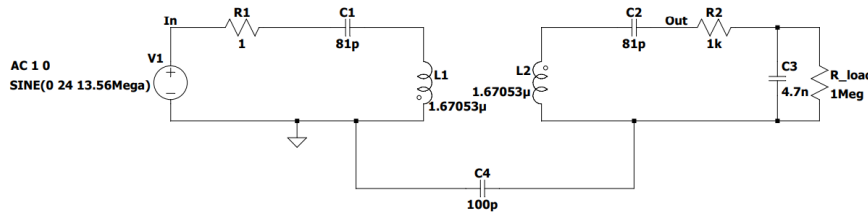


Figure 10: Validation through LTSpice for different values of coupling factor (K).

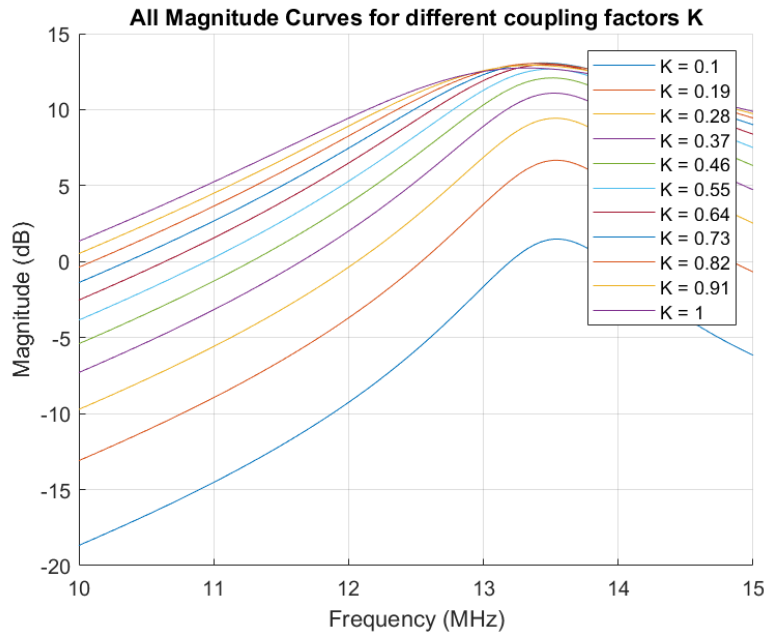


Figure 11: Validation through LTSpice for different values of coupling factor (K).

3.5 Circuit Assembly and Resonance Verification

The components were soldered onto the PCB and the completed circuit was analyzed using a network analyzer as shown in Figure 12.

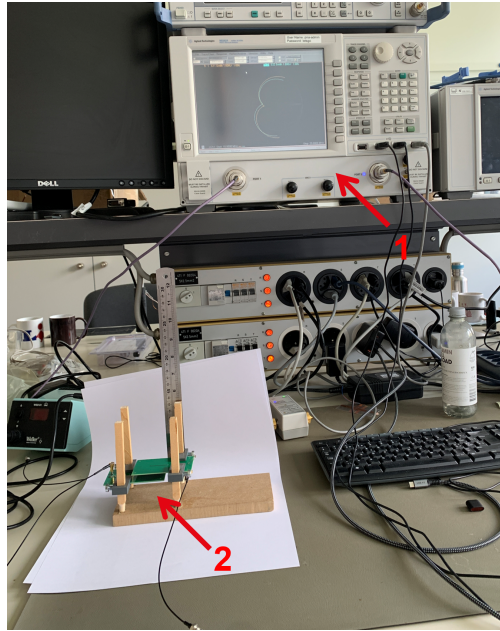


Figure 12: Set-up (2) connected to the network analyzer: : Agilent Technologies, N5242A PNA-X Network Analyzer, 10 MHz - 26.5 MHz (1).

By observing the total impedance on a Smith chart for a single PCB (1), as shown in Figure 13, it becomes apparent that the resonant condition, where the imaginary part of the impedance should be zero (2), is not fully satisfied at the target frequency. In order to satisfy this condition, a fine-tuning step should be performed.

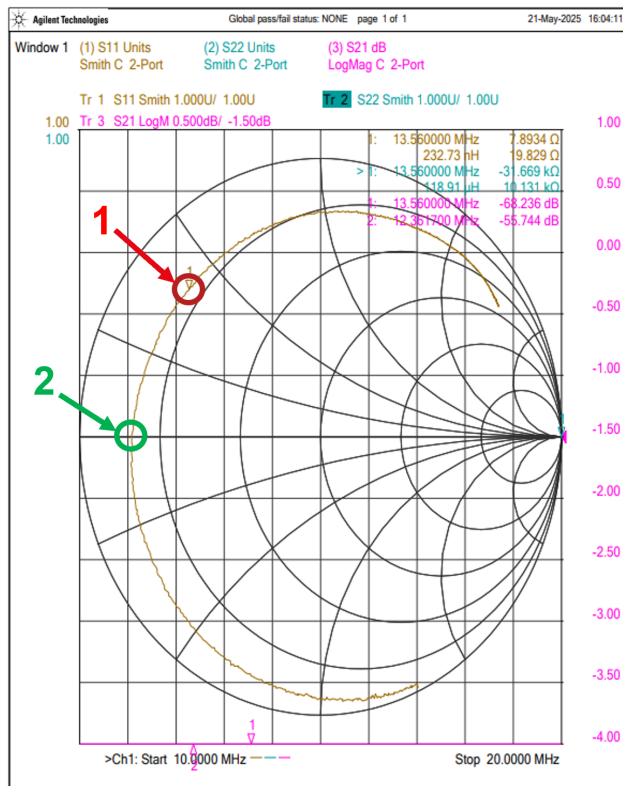


Figure 13: Smith chart of the total impedance obtained at 13.56 MHz (1) for one of the PCB and the expected result once the resonance is achieved at 13.56 MHz.

3.6 Power Transfer Characterization

Finally, the energy transfer performance was measured. Using the network analyzer presented in Figure 12, S-parameters were recorded for the bipole system to analyze signal transmission and reflection. Measurements were first taken without any load to characterize the system's inherent behavior, followed by tests with a load of $1\text{ k}\Omega$ connected to evaluate how it affected the system performance. S-parameter were measured at multiple vertical separations, using the set-up presented in Figure 14, between the coils in order to assess how distance impacts coupling strength and overall energy transfer performance. One misalignment experience was also performed.

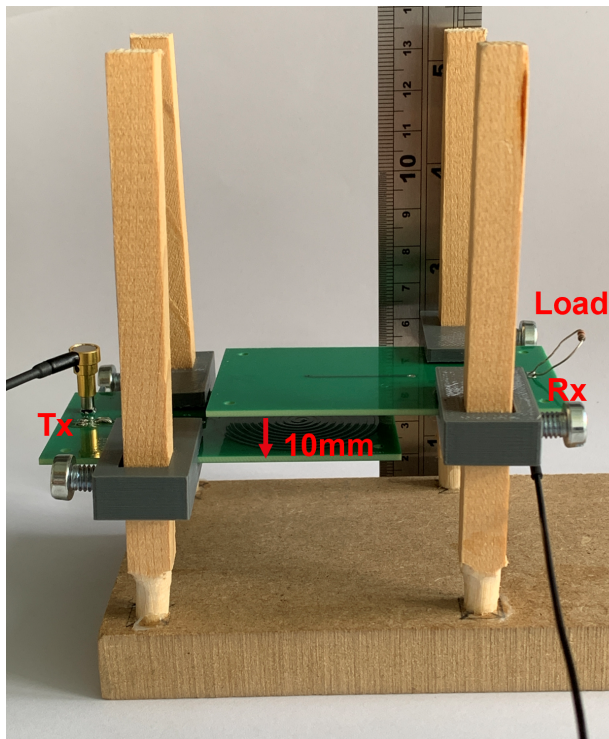


Figure 14: Set-up used to measure the S-parameters at different distances. This corresponds to a separation of 10 mm with a load of $1\text{ k}\Omega$.

3.7 Efficiency Analysis

By using the S-parameters extracted from the unloaded system, we can predict how the system will behave when terminated by any arbitrary load impedance Z_L . This method allows us to analyze the influence of the load on the overall network without performing additional physical measurements.

The network is modeled as a passive linear two ports system described by its scattering matrix \mathbf{S} . With this framework, we calculate important quantities such as the reflected and transmitted waves, the current flowing into the load, the power delivered to it and the efficiency of power transfer.

The following derivation presents the general case. It provides the theoretical foundation to

understand and predict the loaded system's behavior based on the measured S-parameters of the unloaded network. The formulas and methodology are adapted from [3, 18]

$$\begin{bmatrix} b_1 \\ b_2 \end{bmatrix} = \begin{bmatrix} S_{11} & S_{12} \\ S_{21} & S_{22} \end{bmatrix} \begin{bmatrix} a_1 \\ a_2 \end{bmatrix} \quad (3)$$

where :

- a_1, a_2 represent the incident waves at port 1 and port 2 respectively,
- b_1, b_2 represent the reflected waves at port 1 and port 2 respectively,
- S_{ij} are the elements of the scattering (S) matrix obtained from the measure .s2p file.

When port 2 is terminated with a load impedance Z_L , the reflection coefficient at that port is given by:

$$\Gamma_L = \frac{Z_L - Z_0}{Z_L + Z_0} \quad (4)$$

The incident wave at port 2 due to the load is:

$$a_2 = \Gamma_L \cdot b_2 \quad (5)$$

Substitute Eq. (5) into Eq. (3) to express everything in terms of a_1 :

$$b_1 = S_{11}a_1 + S_{12}a_2 = S_{11}a_1 + S_{12}\Gamma_L b_2 \quad (6)$$

$$b_2 = S_{21}a_1 + S_{22}a_2 = S_{21}a_1 + S_{22}\Gamma_L b_2 \quad (7)$$

Solving for b_2 :

$$b_2 = \frac{S_{21}a_1}{1 - S_{22}\Gamma_L} \quad (8)$$

Then:

$$a_2 = \Gamma_L \cdot \frac{S_{21}a_1}{1 - S_{22}\Gamma_L} \quad (9)$$

The input reflection coefficient seen at port 1 is:

$$\Gamma_{\text{in}} = \frac{b_1}{a_1} = S_{11} + \frac{S_{12}S_{21}\Gamma_L}{1 - S_{22}\Gamma_L} \quad (10)$$

The current at port 2 is derived from the wave amplitudes as:

$$I_2 = \frac{a_2 - b_2}{\sqrt{Z_0}} = \frac{(\Gamma_L - 1)b_2}{\sqrt{Z_0}} \quad (11)$$

The RMS current is:

$$I_{2,\text{RMS}} = \frac{|I_2|}{\sqrt{2}} = \frac{|\Gamma_L - 1| \cdot |b_2|}{\sqrt{2Z_0}} \quad (12)$$

The real power delivered to the load is:

$$P_L = |b_2|^2(1 - |\Gamma_L|^2) \quad (13)$$

The input power is:

$$P_{\text{in}} = |a_1|^2(1 - |\Gamma_{\text{in}}|^2) \quad (14)$$

Finally, the power transfer efficiency is:

$$\eta = \frac{P_L}{P_{\text{in}}} \cdot 100\% \quad (15)$$

4 Description of Solutions

This section focuses on the experimental results obtained from Section 3.5 to Section 3.7. Until Section 3.5, the study was primarily based on simulations and confirmations of the results.

Section 3.5 first presents the measured inductance value of the coil, which slightly deviates from the theoretical value. This difference may be due to several factors, such as manufacturing tolerances not accounted for during the design phase or additional inductance from the PCB traces. Following this, an impedance analysis was carried out on a test board to verify whether the resonance condition is satisfied, the imaginary part of the impedance should be zero at the operating frequency. However, this condition was not fully met, as a residual imaginary component of inductive nature was observed.

Two factors may explain this deviation from the initial design:

- High frequency transmission line effects, which alter the signal and introduce non-negligible mismatches.
- Component tolerances: the real-world performance of the inductors and capacitors used deviates from their nominal values, especially at 13.56 MHz.

To cancel out this inductive effect and bring the impedance closer to resonance, a practical approach would be to fine-tune the passive components, particularly by increasing the capacitive value slightly to compensate for the inductance in our case.

In Section 3.6, measurements were taken for different vertical distances between the two coils, ranging from 0 to 10 mm, without any load connected. The S-parameter values (S_{11} and S_{21}) were extracted and summarized in the following figure:

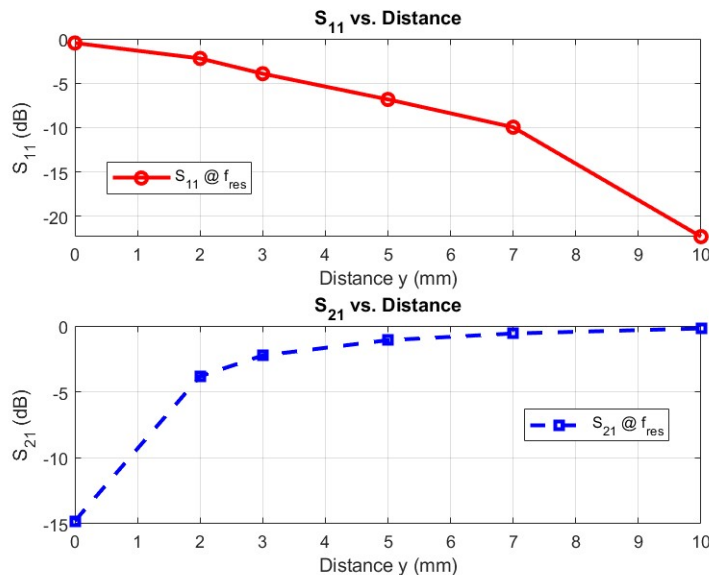


Figure 15: Overall results of the S-parameters for different distances.

A clear trend can be observed:

- At short distances, the parameter S_{11} is high, strong reflection, and S_{21} is low, weak transmission.
- As the distance increases, S_{11} decreases while S_{21} increases.

According to Sample *et al.* [17], this behavior is related to the coupling factor K. At very short distances, the coupling is strong, leading to frequency splitting, which indicated an over-coupled system. This results in high reflection, S_{11} , and low transmission, S_{21} .

As the distance increases, the coupling weakens and the system approaches the critical coupling point, ideal for efficient power transfer. Beyond this point, the system becomes under-coupled and the transmitted power magnitude decreases.

The author in [17] mentions the existence of a critical coupling point, after which the power transfer starts to decline. Since our application does not require distances greater than 10 mm, we can reasonably assume that the critical point is reached around this distance.

The following graph shows the S-parameters measures at 10 mm without a load:



Figure 16: Overall results of the S-parameters at different distances.

From the above graph and the measured values of S_{11} and S_{21} , we can assess whether the system is well matched to the network analyzer's input impedance, which is:

$$Z_0 = 50 \Omega$$

Given the measured reflection coefficient:

$$S_{11}^{\text{dB}} = -22.39 \text{ dB}$$

$$|S_{11}| = 10^{\frac{S_{11}^{\text{dB}}}{20}} = 10^{\frac{-22.39}{20}} \approx 0.076$$

The input impedance seen by the source can be estimated using the following relationship:

$$Z_{\text{in}} = Z_0 \cdot \frac{1 + |S_{11}|}{1 - |S_{11}|} = 50 \cdot \frac{1 + 0.076}{1 - 0.076} = 50 \cdot \frac{1.076}{0.924} \approx 50 \cdot 1.164 \approx 58.2 \Omega \quad (16)$$

This equation provided the input impedance seen by the source as a function of the reflection coefficient. In the case of perfect matching $S_{11} = 0$, the input impedance would equal to $Z_0 = 50 \Omega$.

A calculated value of $Z_{\text{in}} \approx 58.2 \Omega$ indicated good matching, with minimal reflection. However, since this result is obtained without a real load connected, it has limited significance in assessing the system's practical performance. Nevertheless, based on the obtained results, the mutual inductance can be estimated using the S_{21} parameter, following the method described in [7]. The relationship between the impedance Z_{21} and the mutual inductance M_{21} is given by:

$$Z_{21} = j\omega M_{21} \quad (17)$$

Thus, the mutual inductance is calculated as:

$$M_{21} = \frac{\text{Im}(Z_{21})}{\omega} = \frac{\text{Im}(Z_{21})}{2\pi f} \approx 0.577 \mu\text{H} \quad (18)$$

From this value, the coupling factor K between the coils can be determined by:

$$K = \frac{M}{\sqrt{L_1 L_2}} = \frac{M}{L} \quad \text{avec } L_1 = L_2 = L = 1.67053 \mu\text{H} \quad (19)$$

$$K = \frac{0.577 \mu\text{H}}{1.67 \mu\text{H}} \approx 0.345 \quad (20)$$

This coupling factor quantifies the magnetic coupling efficiency between the coils and is a

key parameter in the design.

A misalignment experiment was also performed for a distance of 10 mm without a load as shown in Figures 17 and 18 but will not be part of the discussion as it was not very relevant for the overall analysis. However a comparative result of the transmission S_{21} is provided in Table 4.

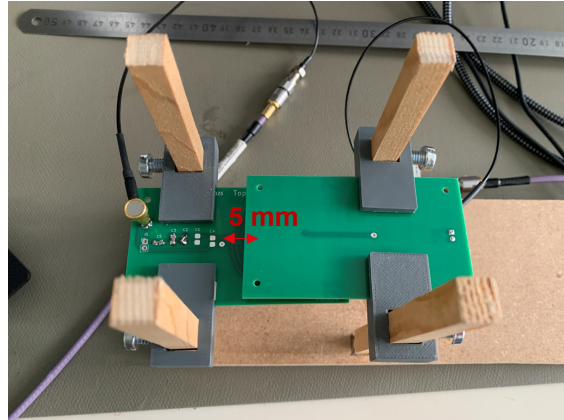


Figure 17: Misalignment experiment using the set-up with a 5 mm offset.

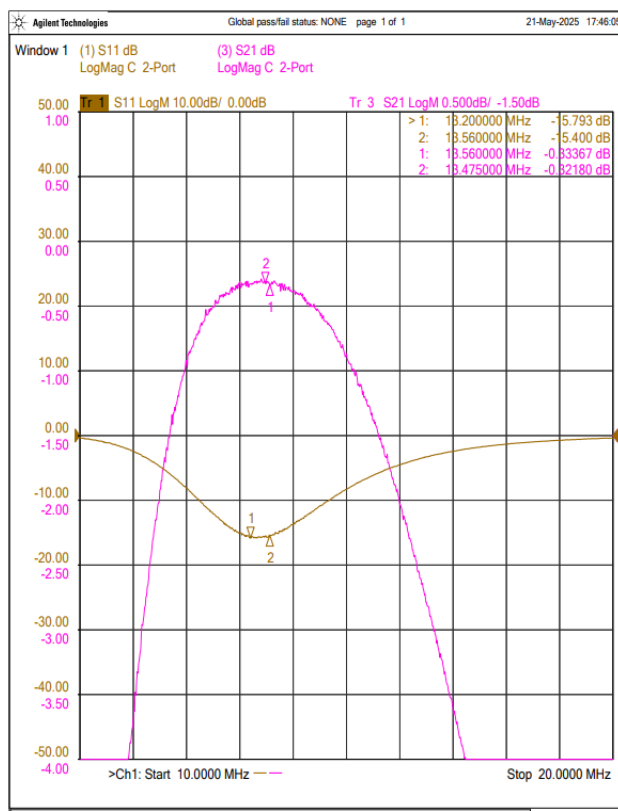


Figure 18: Results obtained for 5 mm offset with the network analyzer.

S_{21} (dB) not misaligned for 10 mm at 13.56 MHz	S_{21} (dB) misaligned for 10 mm at 13.56 MHz
-0.2	-0.33

Table 4: Comparison of S_{21} at 13.56 MHz with and without misalignment.

Repeating the same measurement but now with a $1\text{k}\Omega$ load placed at the receiver, at the same 10 mm distance, yields the following result:

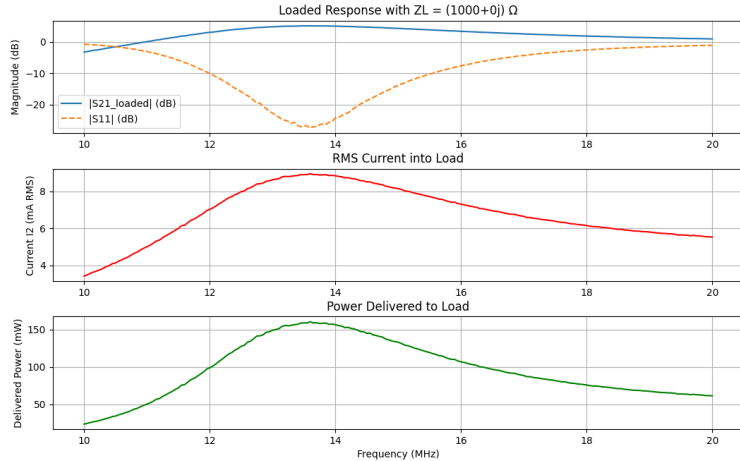


Figure 19: Overall results for a loaded circuit showing the magnitude of the S-parameters, the current (RMS) and the power delivered to the load.

At 13.56 MHz, we have the following results:

$ S_{21} $ (dB)	$ S_{11} $ (dB)	I_2 (mA)	P_{Load} (mW)
5.02	-26.77	8.91	158.76

Table 5: Different results obtained at 13.56 MHz

$$S_{11}^{\text{dB}} = -26.77 \text{ dB}$$

$$|S_{11}| = 10^{\frac{S_{11}^{\text{dB}}}{20}} = 10^{\frac{-26.77}{20}} \approx 0.046$$

Again, using the impedance conversion formula 16, $|Z_{in}| \approx 10.87 \Omega$. This result can be explained by the fact that the impedance seen from the source includes the 50Ω input resistance in parallel with the mutual inductance and also in parallel with the load. This combined parallel resistance reduces the overall value of Z_{in} as seen from the source.

Finally, in Section 3.7, we derived the equations required to compute the system efficiency. However, calculating efficiency without a connected load is not meaningful, as efficiency is defined as the ratio between the power delivered to the load and the power supplied at the input. In the absence of a load, no real power is transferred and the resulting value would not accurately represent the system's performance. Therefore, the efficiency with the load is

$$\eta_{\text{load}} = 57.48 \% \quad (21)$$

5 Comparative Results

The following table summarizes the comparison between the expected theoretical values and the actual results obtained through circuit design and simulation. Most parameters show acceptable deviations, while some fall outside the expected range. A critical discussion will be provided in the following section.

Parameter	Theoretical Value	Measured Value	Relative Error (%)
$L (\mu\text{H})$	1.84	1.6734	9.21
$C_p (\text{pF})$	[2;5]	1.90921	Better than expected
$P_{Load=1k\Omega} (\text{mW})$	[300, 500]	158.76	Out of range (-47.08 vs 300 mW)
$P_{Load=50\Omega} (\text{mW})$	[300, 500]	935.86	Out of range
$I_{2,Load=1k\Omega} (\text{mA})$	10	8.91	10.9
$I_{2,Load=50\Omega} (\text{mA})$	10	96.74	Better than expected
$\eta_{Load=1k\Omega} (\%)$	51.28 (for $K \approx 0.3$)	57.48	Better than expected

Table 6: Comparison between theoretical and measured values

The theoretical efficiency was simulated and Figure 20 shows the maximum achievable efficiency for various values of the coupling factor K . For the measured coupling factor $K \approx 0.3$, the corresponding theoretical maximum efficiency is approximately $\eta_{max,dB} \approx -5.8$.

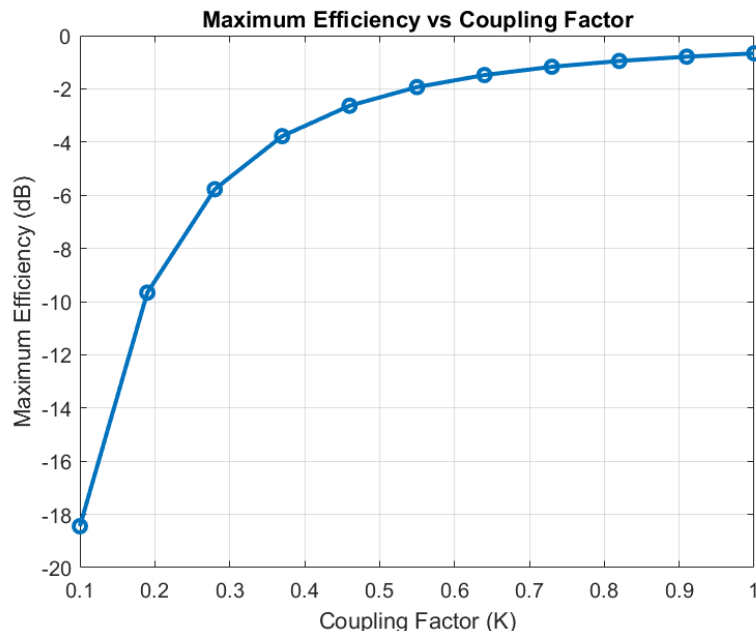


Figure 20: Simulation of the maximum efficiency over the coupling factor K done in the LTSpice step.

6 Critique of Solutions

Several initial assumptions made during the design process were later found to be inaccurate or incomplete, especially considering the precision required in wireless power transfer (WPT) systems operating at high frequencies.

First, the effect of skin depth and proximity effect were neglected in the early stages of the design. Even though the value was closed to 1Ω at the frequency 13.56 MHz if we wanted to achieve higher power transfer and have good efficiency, we should have take into account. As a result, they influence the effective resistance of the coil, increasing power losses and reducing efficiency. Neglecting these effects can lead to an underestimation of resistive losses and an overestimation of the system's quality factor.

Second, the resonant circuit design was carried out without taking the load into account, which is a critical oversight. In practical WPT systems, the presence of a load modifies the total impedance seen by the circuit and alters both the resonant frequency and the power transfer conditions. To accurately model the system, the resonant frequency must include the total capacitance, which consists of both parasitic and load components, as shown in the following expression:

$$f_r = \frac{1}{2\pi\sqrt{L(C_{\text{para}} + C_{\text{load}})}} \quad (22)$$

Furthermore, the presence of the load also contributes to the total series resistance of the system, which directly impacts the quality factor.

$$Q = \frac{\omega_0 L}{R_{\text{total}}} \quad (23)$$

Where the total resistance is given by:

$$R_{\text{total}} = R_{\text{coil}} + R_{\text{load}} \quad (24)$$

These relations highlight the importance of considering the load early in the design process to ensure accurate resonance and optimal power transfer efficiency.

Transmission line effects were not considered in this project. However, at high frequencies and with non-negligible trace lengths, such effects can impact signal integrity and impedance matching. Careful capacitor selection is also necessary to account for parasitics and frequency dependant behavior.

System tuning is inherently iterative, requiring adjustment of component values until the imaginary part of the impedance is near zero, the resonance condition. In this project, such tuning was performed only once, which may limit optimization under real operating conditions.

7 Conclusion

This project focused on the design and simulation of a wireless power transfer (WPT) system operating at 13.56 MHz for biomedical application. Key constraints such as physical size, power requirements and frequency selection were considered early on to ensure feasibility and safety. The chosen frequency provided a practical trade-off between penetration depth, efficiency and tissue safety, while the Rx coil size was kept within the typical range found in biomedical literature to minimize invasiveness.

Throughout the design process, simplified assumptions, such as neglecting skin and proximity effect, transmission line behavior and the influence of the load, enabled an initial prototype. However, these simplifications also introduced deviations between theoretical expectations and the actual performance observed in simulation. Specifically, the resonance conditions and quality factor were significantly affected by parasitic effects and the absence of load consideration during the initial design of the resonant circuit.

The comparison between theoretical and measured values highlighted both acceptable and critical deviations. While some parameters met or exceeded expectations, others such as the power delivered to the load, fell outside the target range, underlining the importance of a more comprehensive modeling approach.

Moving forward, it is essential to adopt more rigorous and iterative design methodology that includes high frequency phenomena and load integration from the beginning. Fine-tuning remains a key step to achieve resonance condition and optimizing system efficiency. These insights will be valuable for future refinement and for the development of a more robust, high performance WPT systems suited for biomedical use.

References

- [1] D. B. Ahire, Vitthal J. Gond, and Jayant J. Chopade. “Compensation topologies for wireless power transmission system in medical implant applications: A review”. In: *Biosensors and Bioelectronics: X* 11 (2022), p. 100180. DOI: 10.1016/j.biosx.2022.100180.
- [2] Surajit Das Barman et al. “Wireless powering by magnetic resonant coupling: Recent trends in wireless power transfer system and its applications”. In: *Renewable and Sustainable Energy Reviews* 51 (2015), pp. 1525–1532. DOI: 10.1016/j.rser.2015.07.031.
- [3] F. Caspers. *RF Engineering Basic Concepts: S-parameters*. Tech. rep. Available online, CERN technical report. CERN, Geneva, Switzerland, 2025. URL: <https://cds.cern.ch/record/1415639/files/p67.pdf>.
- [4] H. Dimis and P. M. Mendes. “A comprehensive review of powering methods used in state-of-the-art miniaturized implantable electronic devices”. In: *Biosensors and Bioelectronics* 172 (2021), p. 112781. DOI: 10.1016/j.bios.2020.112781.
- [5] Mussa Elsaadi et al. “Strongly Coupled Magnetic Resonance based Wireless Power Transfer System for Implantable Medical Devices”. In: *Proceedings of the Faculty of Engineering Conference*. University of Tobruk. Libya, 2023.
- [6] Daniel K. Freeman and Steven J. Byrnes. “Optimal Frequency for Wireless Power Transmission Into the Body: Efficiency Versus Received Power”. In: *IEEE Transactions on Antennas and Propagation* 67.6 (June 2019), pp. 4073–4080. DOI: 10.1109/TAP.2019.2903148.
- [7] Seon-Jae Jeon, Sang-Hoon Lee, and Dong-Wook Seo. “Unilateral Route Method to Estimate Practical Mutual Inductance for Multi-Coil WPT System”. In: *Electronics* 9.2 (2020), p. 385. DOI: 10.3390/electronics9020385.
- [8] Sadeque Reza Khan et al. “Wireless Power Transfer Techniques for Implantable Medical Devices: A Review”. In: *Sensors* 20.12 (2020). Published: 19 June 2020, p. 3487. DOI: 10.3390/s20123487. URL: <https://www.mdpi.com/1424-8220/20/12/3487>.
- [9] Minki Kim and Jungwon Choi. “Design of Self-Resonant Spiral Coils for Mid-Range, High-frequency Wireless Power Transfer Systems”. In: *Proceedings of the IEEE Wireless Power Transfer Conference (WPTC)*. IEEE. Minneapolis, USA, 2023.
- [10] Sunderarajan S. Mohan et al. “Simple Accurate Expressions for Planar Spiral Inductances”. In: *IEEE Journal of Solid-State Circuits* 34.10 (Oct. 1999), pp. 1419–1424. DOI: 10.1109/4.792620.
- [11] Krithikaa Mohanarangam, Yellappa Palagani, and Jun Rim Choi. “Evaluation of Specific Absorption Rate in Three-Layered Tissue Model at 13.56 MHz and 40.68 MHz for Inductively Powered Biomedical Implants”. In: *Micromachines* 10.3 (2019), p. 198. DOI: 10.3390/mi10030198.
- [12] Claudia Pacurar et al. “Adapting the Formula for Planar Spiral Inductors’ Inductance Computation to the New Oval Geometric Shape, Ideal for Designing Wireless Power

- Transfer Systems for Smart Devices". In: *Mathematics* 13.3 (Jan. 2025), p. 348. DOI: 10.3390/math13030348. URL: <https://www.mdpi.com/2227-7390/13/3/348>.
- [13] Chi Dat Pham et al. "Parasitic Capacitance Analysis in High-Frequency Wireless Power Transfer Systems". In: *Proceedings of the IEEE Wireless Power Transfer Conference (WPTC)*. IEEE. Ha Noi, Viet Nam and Espoo, Finland, 2023.
- [14] I. R. E. G. Prazeres, V. Prasanth, and P. Bauer. "Multi-coil multi-frequency inductive power transfer". In: *2015 IEEE Vehicle Power and Propulsion Conference (VPPC)*. IEEE. 2015, pp. 1–6. DOI: 10.1109/VPPC.2015.7352930.
- [15] Masood Rehman, Perumal Nallagownden, and Zuhairi Baharudin. "Efficiency Investigation of SS and SP Compensation Topologies for Wireless Power Transfer". In: *International Journal of Power Electronics and Drive System (IJPEDS)* 10.4 (Dec. 2019), pp. 2157–2164. ISSN: 2088-8694. DOI: 10.11591/ijpedes.v10.i4.2157-2164. URL: <http://iaescore.com/journals/index.php/IJPEDS>.
- [16] S. Saat et al. "The Development of Wireless Power Transfer Technologies for Low Power Applications: An Acoustic Based Approach". In: *Journal of Telecommunication, Electronic and Computer Engineering (JTEC)* 7.2 (2015), pp. 129–135. URL: <https://jtec.utm.edu.my/jtec/article/view/624>.
- [17] Alanson P. Sample, David A. Meyer, and Joshua R. Smith. "Analysis, Experimental Results, and Range Adaptation of Magnetically Coupled Resonators for Wireless Power Transfer". In: *IEEE Transactions on Industrial Electronics* 58.2 (2011), pp. 544–554. DOI: 10.1109/TIE.2010.2061362.
- [18] M. Stanculescu et al. "Using S Parameters in Wireless Power Transfer Analysis". In: *Univ. Politehnica of Bucharest* (2025). Available at: marilena.stanculescu@upb.ro, laviniabobaru@yahoo.com, mihai.iordache@upb.ro, dragos.niculae@upb.ro, victor.bucata@upb.ro.
- [19] Igor Stefanini. "Méthodologie de conception et optimisation d'actionneurs intégrés sans fer". Ph.D. Thesis. Lausanne, Switzerland: École Polytechnique Fédérale de Lausanne (EPFL), 2006.
- [20] Tom Van de Steene et al. "Optimal Frequency and Wireless Power Budget for Miniature Receivers in Obese People". In: *Sensors* 22.13 (2022), p. 4876. DOI: 10.3390/s22134876.